EES Batteries

PAPER

View Article Online
View Journal | View Issue

Cite this: *EES Batteries*, 2025, **1**, 1626

Low-carbon upcycling of vanadium slag into doped cathodes for high-performance zinc batteries

Lin Guo,[a,b,c] Wenting Jia,[a,b,c] Junmei Zhao,[b,c] Gaojie Xu,[a,c] Pengge Ning *[a,b,c] and Hongbin Cao *[a,b,c]

Developing sustainable aqueous energy storage systems is crucial for advancing renewable energy utilization. Herein, a short-process strategy that integrates vanadium metallurgy and material preparation to synthesize high-performance cathodes is proposed for aqueous zinc batteries. By selectively removing harmful impurities from vanadium-slag leachate while utilizing beneficial impurities as dopants, NH_4^+-intercalated and metal-doped V_2O_5 (NHVO-M_x) is efficiently synthesized. The resulting material exhibits enhanced Zn^{2+} diffusion kinetics due to its expanded interlayer spacing and low crystallinity structure, while its reduced bandgap significantly accelerates electron transfer. It delivers a high specific capacity of 454.4 mAh g^{-1} at 0.1 A g^{-1} and maintains 86.6% capacity retention after 3000 cycles at 8 A g^{-1}. Furthermore, this material is employed in a pouch cell, achieving a capacity exceeding 0.39 Ah. This innovative approach reduces costs by 40% and lowers carbon emissions by over 65% by efficiently utilizing inherent impurities instead of relying on conventional chemical additives. It not only simplifies the purification process but also enhances the battery's capacity and sustainability. This work establishes a green, streamlined synthesis paradigm for next-generation aqueous batteries by converting industrial waste impurities into valuable functional components.

Received 11th August 2025,
Accepted 4th October 2025

DOI: 10.1039/d5eb00146c

rsc.li/EESBatteries

Broader context

With the rise of renewable energy, there is an increasing need for efficient and environmentally friendly battery technologies. Aqueous Zn–V-based batteries, known for their safety and low cost, present a promising solution. However, traditional vanadium-based cathodes face inherent limitations, including sluggish zinc-ion diffusion and low electronic conductivity, which result in poor energy storage performance and cycling stability. Although optimization strategies such as doping and interface engineering have yielded some improvements, zinc-ion batteries still fall short for practical applications and often involve complex, costly, and environmentally harmful synthesis. In this work, we propose an innovative, low-carbon synthesis method that abandons the traditional "vanadium purification-doping" process; instead it efficiently utilizes inherent impurities from vanadium sources as dopants. This method results in a novel vanadium-based cathode material, featuring ammonium-ion intercalation and multi-metal doping (denoted as NHVO-M_x). Thanks to the NH_4^+-regulated interlayer spacing and multi-metal-introduced band structure engineering, the material exhibits enhanced structural stability and improved reaction kinetics, leading to high capacity and stable performance. Furthermore, our approach significantly reduces both manufacturing costs and carbon emissions, representing a major step forward in both high-performance Zn-ion battery cathode design and low-carbon material synthesis.

Introduction

The accelerated advancement and efficient utilization of renewable energy have been recognized as critical pathways to realize the strategic goal of carbon neutrality.[1,2] Concurrently, the demand for safe and environmentally friendly energy storage systems is rising, underscoring the need for the development of high-energy-density batteries derived from sustainable resources.[3] Aqueous zinc-ion batteries (AZIBs) are gaining attention as promising candidates for the next generation of energy storage systems, due to their enhanced safety, low cost, competitive performance, and environmental friendliness.[4,5] The exploration of cathode materials with excellent structure, favourable stability, and high capacity is critical to the progress of AZIBs.[5–7] Various materials have been considered as cathodes for AZIBs, including manganese oxides, Prussian blue analogues, vanadium-based materials, and organic compounds.[8–14] Among these, vanadium oxides are particu-

[a]*Chemistry & Chemical Engineering Data Centre, Institute of Process Engineering, Chinese Academy of Sciences, Beijing 100190, P. R. China. E-mail: pgning@ipe.ac.cn, hbcao@ipe.ac.cn*
[b]*School of Chemical Engineering, University of Chinese Academy of Sciences, Beijing 100049, China*
[c]*Institute of Process Engineering, Chinese Academy of Sciences, Beijing 100190, China*

larly noted due to their rich valence states ($V^{5+} \leftrightarrow V^{2+}$) and open framework structure, which contribute to their high theoretical capacity and considerable potential for application.[15,16] However, the performance of vanadium pentoxide is hindered by its intrinsic low conductivity and sluggish diffusion kinetics.[17,18] Recent studies have shown that ion pre-intercalation or doping of the host is an effective strategy to modify its electronic and structural properties, ultimately improving the capacity and stability of AZIBs.[19,20]

The doping of various metal cations, such as Li^+, Na^+, Mg^{2+}, Ca^{2+}, Co^{2+}, Al^{3+}, and Mn^{2+}, into vanadium-based cathodes has been demonstrated to significantly enhance their performance.[21–28] Compared to single-cation modification, multi-ion doping has been shown to produce synergistic effects.[29,30] Moreover, the design of new materials places less emphasis on economic feasibility and environmental effects. The conventional synthesis methods for doping-modified vanadium-based materials typically use commercial high-purity vanadium oxide as the vanadium source, with metal salts acting as doping agents.[21,31] Therefore, it is encompassed within the life cycle of the cathodes, from vanadium slag leachate to high-purity vanadium, involving a sequence of vanadium precipitation, filtration, and re-dissolution *via* heating, or alternatively, a multi-stage solvent extraction process, followed by washing and stripping.[32–34] From a comprehensive perspective, the traditional synthesis strategy involves a lengthy process, high carbon emissions, and considerable environmental concerns. Additionally, the deep impurity removal and doping stages require the use of numerous chemicals, leading to increased costs. Therefore, developing cost-effective and environmentally sustainable preparation methods with shorter processes for vanadium-based cathodes is necessary.

Given the similarity between doping ions and impurities in leachate, we propose selectively utilizing beneficial impurities as dopants in the synthesis of vanadium oxides, thereby enabling a short, low-carbon route for producing doped vanadium-based cathodes. This process involves targeted impurity removal from vanadium slag leachate, without stringent standards for beneficial impurities, followed by precipitation and low-temperature calcination. The strategy successfully synthesizes V_2O_5 doped with multiple elements such as Cr, Ca, and K, and intercalated with NH_4^+ (denoted as NHVO-M_x). These modifications reduce the band gap, significantly accelerating electron transfer, which is crucial to enhance electrochemical performance. Additionally, the NH_4^+-induced expansion of interlayer spacing and the low crystallinity structure further enhance diffusion kinetics at the cathode, contributing to superior (dis-)charge efficiency. Notably, the NHVO-M_x cathode demonstrates a high specific capacity of 454.4 mAh g^{-1} at 0.1 A g^{-1} and excellent cycling stability, retaining 86.6% of its capacity after 3000 cycles at 8 A g^{-1}. Moreover, this material is also used in a pouch cell, delivering a capacity over 0.39 Ah. A multi-objective assessment from both economic and environmental perspectives reveals that the short-process route not only reduces costs and environmental impact but also lowers carbon emissions compared to conventional cathode design.

Results and discussion

Low-carbon short-process synthesis of doped vanadium oxides

The analysis of the alkaline leachate from vanadium slag by inductively coupled plasma optical emission spectrometry (ICP-OES) revealed the coexistence of multiple impurity elements such as V, Cr, Si, and K (Table S1, SI). In conventional synthesis of doping-modified vanadium oxides, vanadium slag leachate undergoes a multi-step deep impurity removal process to produce high-purity vanadium, which is then doped with external dopants and subjected to hydrothermal synthesis (Fig. S1a, SI). However, this process requires a long process and multiple reagents, resulting in high emissions. We propose a novel approach that utilizes the impurities as natural dopants, which are potentially beneficial for energy storage performance, integrating metallurgy and material synthesis. This method synthesizes vanadium oxides with efficient metal ion doping through a low-carbon emission, short-process route (Fig. 1a and Fig. S1b, SI). To assess whether these elements are advantageous within their natural concentration ranges in the leachate, energy storage performance tests were conducted on materials synthesized *via* vanadium precipitation and low-temperature calcination from simulated leachates containing each element individually (as detailed in Experimental section, SI). Compared to the $(NH_4)_{0.24}V_2O_5$ (denoted as NHVO) synthesized from deeply purified leachate, the energy storage performance of NHVO-Cr, NHVO-Ca, and NHVO-K (synthesized from leachates containing Cr, Ca, and K, respectively, in their actual concentration ranges) was significantly superior (Fig. S2, SI). For example, these materials showed a higher first-cycle capacity compared to NHVO at 0.2 A g^{-1}, and their capacity improved after rate capability testing when the current density was returned to 0.2 A g^{-1} (Fig. 1b and c). However, the performance of NHVO-Si, synthesized from Si-containing leachate, significantly declined as the silicon concentration increased. When the Si concentration exceeded 0.1 g L^{-1}, the capacity at 0.2 A g^{-1} notably decreased after rate capability testing (Fig. 1c), suggesting that excessive silicon negatively impacts performance. To address this, the Si concentration in the leachate can be reduced to below 0.02 g L^{-1} using a desilication agent, while other main metal ions remain largely unchanged (Table S2, SI). The resulting multi-element co-doped NHVO (NHVO-M_x), derived from a desiliconized solution with average multi-element concentrations, exhibits superior energy storage capacity compared to the individual doping of each element, achieving 439.1 mAh g^{-1} at 0.2 A g^{-1} (Fig. 1d).

Furthermore, the multi-element co-doped cathodes prepared at varying actual concentrations demonstrated equally impressive performance, showcasing the flexible concentration requirements of the leachate's beneficial impurities (Table S3 and Fig. S3, SI). Therefore, the first step focuses on targeted

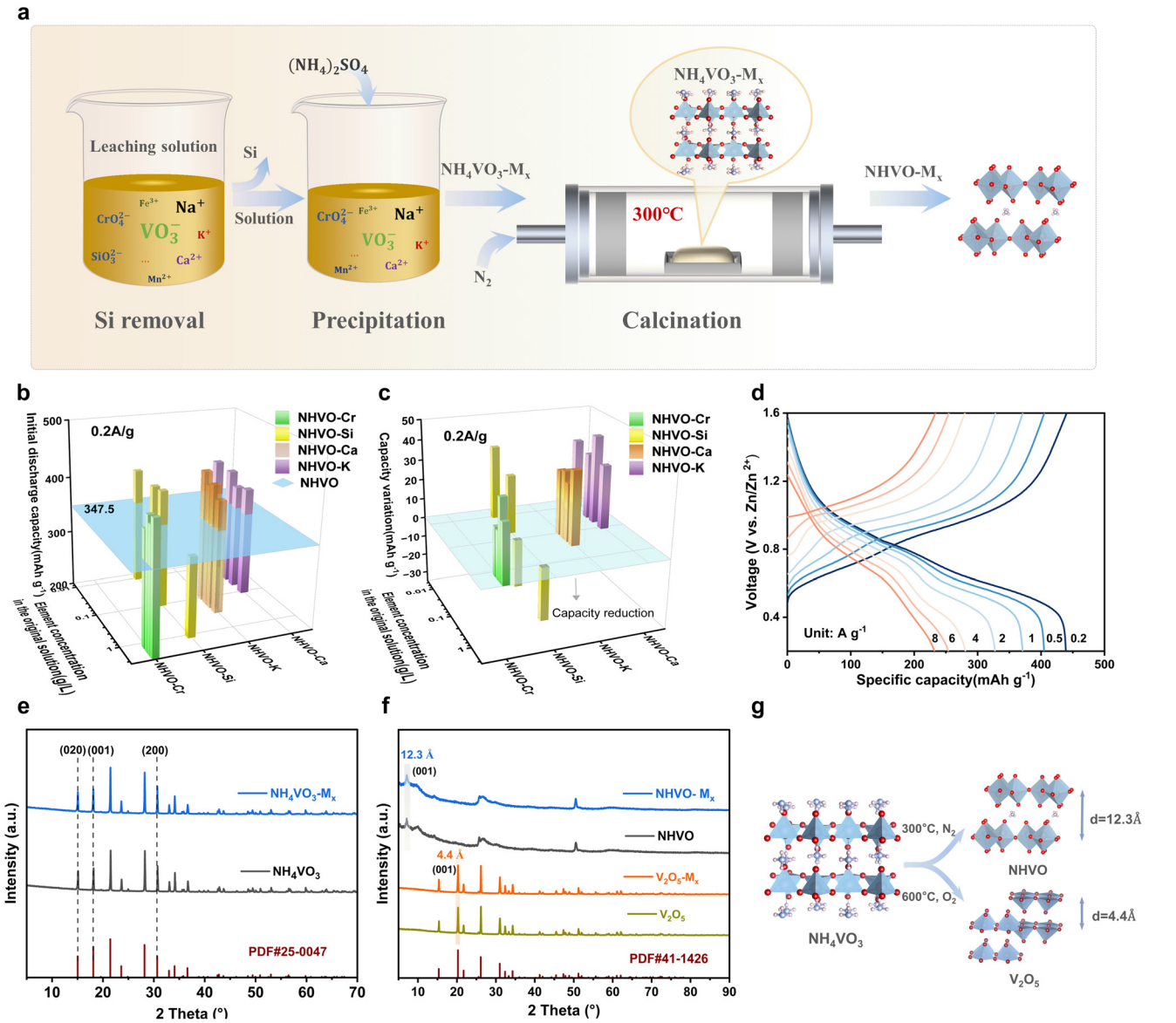

Fig. 1 Short-process synthesis of NHVO-M_x. (a) Schematic of the low-carbon short-process synthesis from vanadium slag leachate to NHVO-M_x. (b) First-cycle capacities of NHVO-Cr, NHVO-Si, NHVO-Ca, and NHVO-K, synthesized from leachates containing Cr, Si, Ca, and K within actual concentration ranges, respectively, as cathodes for AZIBs at 0.2 A g^{-1}. (c) The change in capacity at 0.2 A g^{-1} before and after the rate test for NHVO-Cr, NHVO-Si, NHVO-Ca, and NHVO-K. (d) Rate performance of NHVO-M_x synthesized from leachate after silica removal. (e) XRD patterns of vanadium precipitation precursors from leachates with and without impurity metal ions. (f) XRD patterns of NHVO(-M_x) obtained by calcination of vanadium precipitation precursors at 300 °C under a nitrogen atmosphere, and V_2O_5(-M_x) obtained by calcination at 600 °C under an air atmosphere. (g) Schematic of NHVO and V_2O_5 obtained from precursors NH_4VO_3 under different calcination conditions.

desilication of the leachate, without the need for deep impurity removal or achieving the high-purity standards listed in Table S4 (SI), significantly reducing reagent and energy consumption during the purification process. Subsequently, an ammonium salt is added to the desilicated leachate to precipitate vanadium, yielding NH_4VO_3 doped with various elements (NH_4VO_3-M_x). X-ray diffraction (XRD) shows that all diffraction peaks are consistent with NH_4VO_3, indicating that the trace multi-element doping does not significantly alter the NH_4VO_3 crystal structure (Fig. 1e). In the last calcination step, to determine the optimal conditions, we investigated the structure and performance of vanadium oxides obtained from NH_4VO_3 under different conditions. The XRD results reveal that the product calcined at 600 °C under an oxygen atmosphere, under conventional vanadium product calcination conditions, is orthorhombic V_2O_5 with an interplanar spacing of 4.4 Å for the (001) plane. In contrast, the product calcined at 300 °C under a nitrogen atmosphere is NHVO with some NH_4^+ retained, exhibiting an expanded plane spacing of 12.3 Å, along with improved performance compared to V_2O_5 (Fig. 1f

and g and Fig. S4, SI). Moreover, Tables S5, 6 and Fig. S5–7 (SI) provide a detailed analysis of how calcination temperature (250 °C, 300 °C, 350 °C) and duration (1.5 h, 2 h, 3 h) affect the crystal structure and energy storage performance of vanadium oxides. The results indicate that calcining in nitrogen at 300 °C for 2 hours yields vanadium oxides with optimal NH_4^+ retention and enhanced stability. Additionally, this low-temperature calcination, as opposed to the high-temperature calcination typically used in V_2O_5 synthesis, reduces energy consumption and carbon emissions. Thus, we propose an environmentally friendly synthesis route for doped-vanadium oxide materials derived from vanadium slag leachate. This method involves three steps: (1) selective removal of Si from the vanadium slag leachate, (2) addition of ammonium salts to produce multi-element doped NH_4VO_3, and (3) low-temperature calcination under nitrogen to form vanadium oxides intercalated with NH_4^+ and doped with multiple elements (NHVO-M_x). Compared to traditional methods for synthesizing doped vanadium oxides, this approach significantly shortens the process, reduces the need for large quantities of reagents and energy, and lowers both carbon emissions and costs.

Crystal structure and electronic structure

The XRD patterns in Fig. 1f reveal that the diffraction peaks of NHVO-M_x are consistent with those of NHVO. A prominent diffraction peak appears at 7.1°, and another peak is observed at its integer multiple, 14.2°, indicating that NHVO-M_x possesses a well-defined layered structure with a substantial interlayer spacing of 12.3 Å. This expansion of the interlayer spacing is attributed to the intercalation of NH_4^+ caused during low-temperature calcination.[35] The increased interlayer distance facilitates the reversible intercalation and extraction of zinc ions. To further investigate the incorporation of NH_4^+ between the layers, Raman spectroscopy and Fourier-transform infrared spectroscopy (FT-IR) were performed. Raman spectra showed a slight redshift in the V═O stretching vibration and V–O–V interlayer bending vibration peaks for NHVO-M_x compared to V_2O_5, indicating a subtle elongation of the V═O bonds along the *c*-axis (Fig. 2a). Additionally, FT-IR analysis identified a characteristic NH_4^+ peak, and the redshift in the V═O and V–O–V vibration peaks, suggesting the insertion of NH_4^+ between the layers and interactions with lattice oxygen (Fig. 2b). Scanning electron microscopy (SEM) images and energy dispersive X-ray spectroscopy (EDS) showed the micron-sized NHVO-M_x with a uniform distribution of V, O, N, and Cr, supporting the successful intercalation of NH_4^+ and doping with metal ions (Fig. 2c). However, some trace metal elements were present in such low amounts that they were undetectable by EDS. To obtain quantitative data on the doped elements in the NHVO-M_x, the material was dissolved and analysed by ICP.

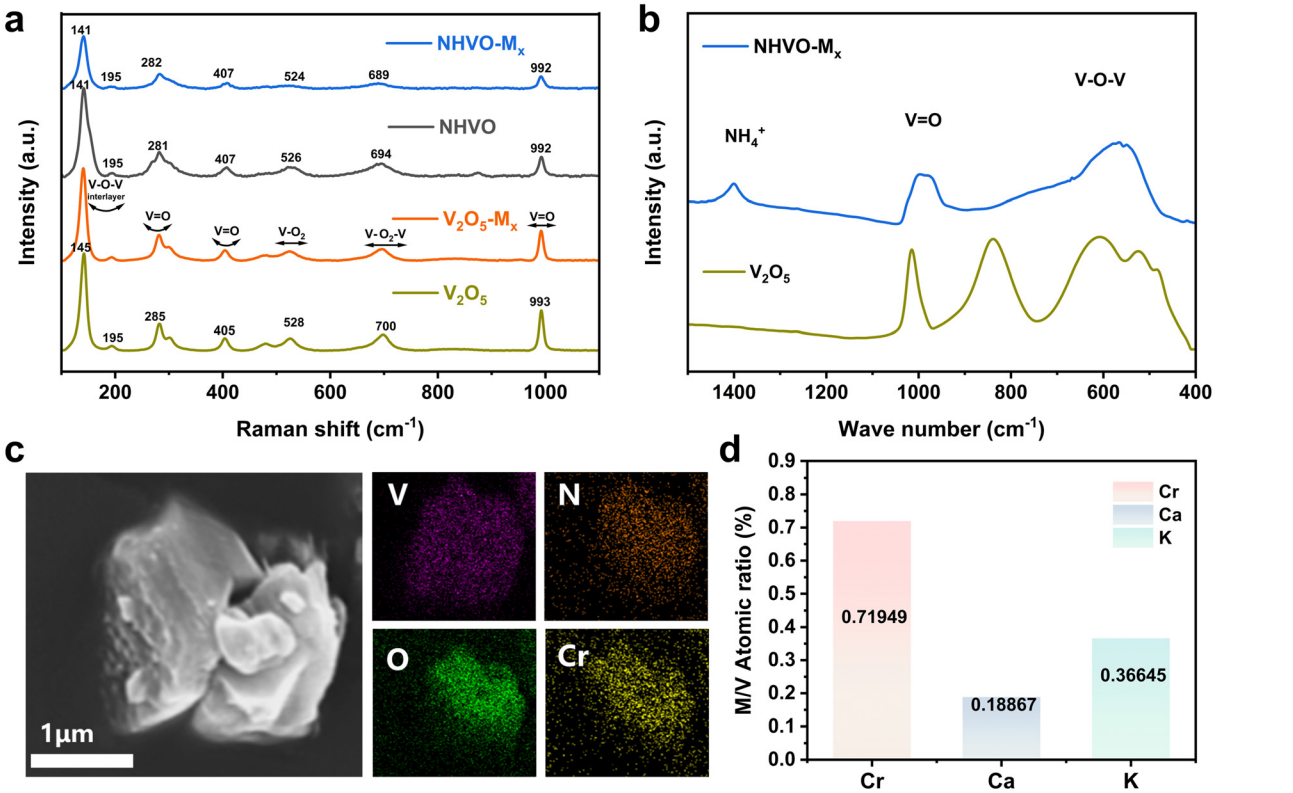

Fig. 2 Structural characteristics of NHVO-M_x. (a) Raman spectra of NHVO(-M_x) and V_2O_5(-M_x). (b) FT-IR spectra of NHVO-M_x and V_2O_5. (c) SEM image and EDS mapping of NHVO-M_x. (d) The atomic ratios of impurity metals to vanadium are calculated from the elemental concentrations measured by ICP-OES after the complete dissolution of NHVO-M_x.

The atomic ratios of Cr/V, Ca/V, and K/V were 0.72%, 0.19% and 0.37%, respectively, confirming that the primary impurity elements from the leachate were successfully doped into the NHVO-M_x for use as cathodes in aqueous zinc batteries (Fig. 2d).

As observed in X-ray photoelectron spectroscopy (XPS), some of the V^{5+} ions were reduced to V^{4+} in NHVO-M_x to maintain electrical neutrality. The peaks at 516.1 and 517.4 eV correspond to the V $2p_{3/2}$ electrons of V^{4+} and V^{5+} respectively (Fig. 3a). This partial reduction of V^{5+} promoted electron transfer. The high-resolution XPS showed that the characteristic peak of lattice oxygen in the O 1s spectrum shifted from 529.8 eV to 530.2 eV, suggesting an interaction between the interlayer NH_4^+ and the lattice oxygen (Fig. 3b). Additionally, the doping of guest elements typically leads to the formation of oxygen vacancies, as indicated by the peak at 531.4 eV in the O 1s spectrum. Based on the peak area, the proportion of oxygen vacancies in NHVO-M_x was found to increase to 31.4%. To further confirm the oxygen vacancy structure, Electron Paramagnetic Resonance (EPR) measurements were performed. As shown in Fig. 3c, V_2O_5 exhibits a weak signal, while NHVO and NHVO-M_x display stronger symmetric peaks at $g \approx 2.00$, corresponding to the characteristic signal of oxygen vacancies. This indicates that the intercalation of ammonium ions and the doping of metals promote the increase of oxygen vacancies. EPR tests were also conducted on NHVO with individual metal doping, and it was found that the oxygen vacancy concentration increased more significantly with the doping of K (Fig. S8, SI). The sample doped with Cr showed a broader characteristic peak, which may be attributed to the changes in the local electronic environment of the oxygen vacancies. These oxygen defects reduced the interaction between zinc

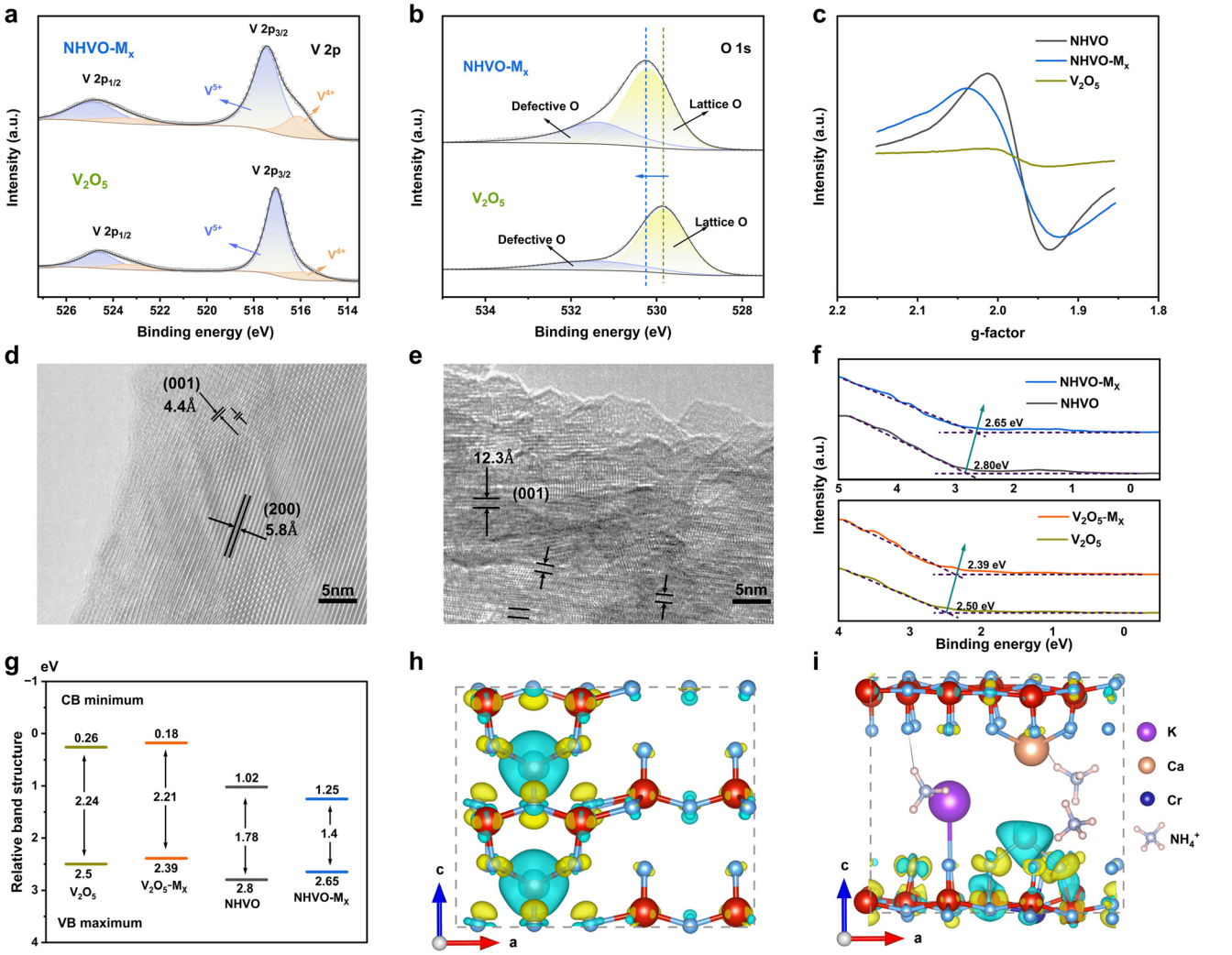

Fig. 3 Structure and electronic structure of NHVO-M_x. (a and b) High-resolution XPS spectra of NHVO-M_x: (a) V 2p and (b) O 1s. (c) EPR spectra of NHVO(-M_x). (d and e) HRTEM images of (d) V_2O_5 and (e) NHVO-M_x. (f) Valence band structures of NHVO(-M_x) and V_2O_5(-M_x). (g) Energy band structures of NHVO(-M_x) and V_2O_5(-M_x). (h and i) Differential charge densities with Zn-ion intercalation in (h) V_2O_5 and (i) NHVO-M_x. The yellow and cyan regions represent charge accumulation and depletion, respectively. The isosurface value is 0.003 e per $bohr^3$.

ions and the lattice, thereby facilitating ion diffusion. In high-resolution transmission electron microscopy (HRTEM), V_2O_5 exhibited clear lattice fringes and narrow spacings (Fig. 3d). NHVO-M_x with intercalated NH_4^+ showed an interlayer spacing of 12.3 Å and a polycrystalline structure of low crystallinity (Fig. 3e). Moreover, the selected area electron diffraction (SAED) pattern of NHVO-M_x displayed concentric rings formed by multiple points, corresponding to a polycrystalline structure. In contrast, the diffraction pattern of V_2O_5 consisted of bright diffraction spots, indicating a high degree of crystallinity (Fig. S9, SI). This suggested that NHVO-M_x possessed a more disordered crystal structure. The low crystallinity of NHVO-M_x provided additional diffusion pathways and active sites, effectively alleviating the structural stress caused by ion intercalation.[36]

To further investigate the effects of NH_4^+ and various metal ions on the electronic structure of the material, XPS valence band measurements were performed. We analysed the relative positions of the valence band (VB) maxima for V_2O_5, V_2O_5-M_x, NHVO, and NHVO-M_x. Metal doping shifted the valence band edge of V_2O_5 from 2.50 eV to 2.39 eV and the valence band edge of NHVO from 2.80 eV to 2.65 eV, thereby enhancing the maximum energy edge (Fig. 3f). To further elucidate the electronic properties at the interface, we employed UV–visible diffuse reflectance spectroscopy (UV-vis DRS) to investigate the band structure of V_2O_5 with and without NH_4^+ intercalation and metal doping. V_2O_5 without doping or intercalation exhibited the widest band gap. NH_4^+ intercalation led to a reduction in the overall band structure and narrowed the band gap. Compared to the 1.78 eV bandgap of NHVO, doping with different metals further reduced the bandgap, with Ca metal doping contributing a more significant reduction. Additionally, co-doping with multiple metal ions generates a synergistic effect, resulting in a narrower bandgap of 1.4 eV for NHVO-M_x (Fig. 3g and Fig. S10, 11, SI). The role of NH_4^+ intercalation and metal doping in modulating the electronic structure was further investigated using Density Functional Theory (DFT). The total densities of states of V_2O_5 and NHVO-M_x are shown in Fig. S12 (SI). Compared to V_2O_5, NHVO-M_x exhibited a narrower band gap, and the Fermi level shifted from the top of the valence band to higher density states. This suggested that the intercalation of NH_4^+ and metal doping improve the electronic conductivity, which is beneficial for electron transfer during electrochemical reactions. The differential charge density showed the interaction between the cathode and the inserted zinc ions. Fig. 3h and i show that V_2O_5 demonstrated a strong interaction with the Zn^{2+}, indicating that the insertion/extraction of Zn^{2+} was relatively difficult, with slow diffusion rates. In contrast, the improvement in crystal and electronic structures significantly weakened the electrostatic interaction between NHVO-M_x and Zn^{2+}, which benefited the zinc ion diffusion dynamics. In conclusion, the proposed eco-friendly short-process strategy effectively utilizes metal ion doping and NH_4^+ intercalation to improve both the crystal and electronic structures, promoting charge transfer and ion diffusion, thus benefiting NHVO-M_x with excellent electrochemical performance.

Kinetic mechanism and zinc storage performance

Intercalation and element doping can modify the structure and electronic properties of metal oxides. The resulting increase of interlayer spacing and low crystallinity structures facilitate ion diffusion, and the reduced bandgap accelerates charge transfer, which in turn boosts electrochemical activity. To verify the enhancement of ion transport properties in the electrode, the Zn^{2+} diffusion coefficients ($D_{Zn^{2+}}$) of cathodes were measured using the galvanostatic intermittent titration technique (GITT, Fig. S13a, SI). The results indicated that the $D_{Zn^{2+}}$ in the NHVO-M_x cathode ranged from 10^{-9} to 10^{-11} cm^2 s^{-1}, which was slightly higher than that in NHVO and significantly higher than that in the V_2O_5 cathode (10^{-10} to 10^{-13} cm^2 s^{-1}) (Fig. 4a). This suggested that the enhanced ion diffusion was primarily attributed to the increased interlayer spacing caused by the intercalation of NH_4^+. The doping of metal ions also played a role in enhancing the diffusion of zinc ions within the material to a certain extent (Fig. S13b, SI). To further investigate the effects of metal ion doping on the ionic diffusion and electron transfer properties of NHVO-M_x electrodes, electrochemical impedance spectroscopy (EIS) was conducted. The semicircle in the high-frequency region corresponds to charge transfer resistance, while the linear tail in the low-frequency region represents the ionic diffusion process. An equivalent circuit was fitted to the test results, which includes solution resistance (R_s), double-layer capacitance (Q), charge transfer resistance (R_{ct}), and diffusion impedance (W_o) (Fig. 4b). It was found that NHVO-M_x had an R_{ct} of 62.7 Ω, whereas the undoped NHVO electrode exhibited a higher R_{ct} of 294 Ω. This indicates that doping with multiple metal ions of Cr, Ca, and K reduces the charge transfer resistance of the cathode. The steep slope in the low-frequency region and the low diffusion impedance further confirm the superior ionic diffusion capability of NHVO-M_x. The results from the GITT and EIS tests indicate that the incorporation of NH_4^+ into NHVO-M_x primarily enhances $D_{Zn^{2+}}$, while multi-metal doping primarily lowers its R_{ct}. The combination of these factors improves charge transfer at the interface and ionic diffusion within the material, leading to an outstanding electrochemical performance.

Further analysis of the cyclic voltammetry (CV) curves of NHVO-M_x was conducted to examine the electrochemical kinetics of Zn^{2+} storage. In Fig. 4c, at a scan rate of 0.2 mV s^{-1}, the two reversible redox pairs at 0.56/0.75 V and 0.84/1.07 V correspond to the two-step (de)intercalation of Zn^{2+} during charge storage. The reduction peaks at 0.84 V and 0.56 V reflect the conversion of V^{5+} to V^{4+} and V^{4+} to V^{3+}, respectively, with simultaneous Zn^{2+} insertion. The oxidation peaks correspond to the reverse processes, where vanadium is oxidized from V^{3+} to V^{4+} and then to V^{5+}, and Zn^{2+} is de-inserted from the cathode. As shown in Fig. S14a (SI), when the scan rate increased from 0.2 mV s^{-1} to 1.2 mV s^{-1}, the CV curves retained their original shape. Due to polarization, the oxidation peaks shifted to

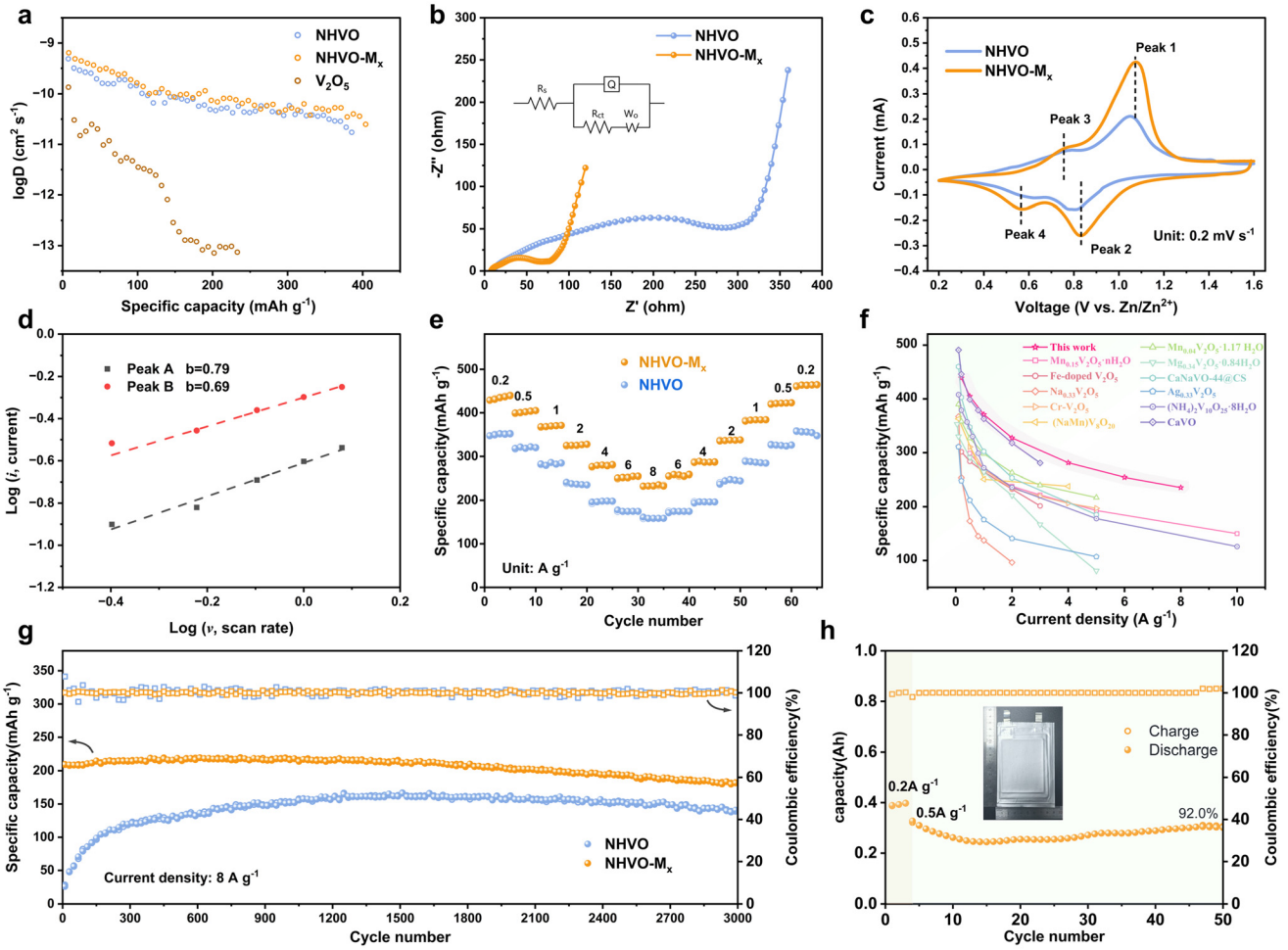

Fig. 4 Electrochemical performance and kinetics of Zn/NHVO-M_x batteries. (a) Zinc ion diffusion coefficients of NHVO-M_x, NHVO, and V_2O_5 calculated from GITT results. (b) EIS curves of NHVO-M_x and NHVO. (c) Typical CV curves of NHVO-M_x and NHVO at a scan rate of 0.4 mV s^{-1}. (d) Peak current of NHVO-M_x *versus* scan rate. (e) Rate performance of NHVO-M_x and NHVO. (f) Comparison of the performance of NHVO-M_x with other vanadium-based cathodes from the literature. (g) Stability test of NHVO-M_x and NHVO at 8 A g^{-1}. (h) The performance of NHVO-M_x in soft-pack batteries.

higher voltages and the reduction peaks shifted to lower voltages. The relationship between the peak current (i) and the scan rate (v) generally follows eqn (1):

$$i = av^b \quad (1)$$

Here, a and b are adjustable. In NHVO-M_x, the b values for the oxidation peak A and the reduction peak B are 0.79 and 0.69, respectively (Fig. 4d). Therefore, the Zn^{2+} storage process in NHVO-M_x is primarily controlled by a mixed mechanism of capacitive response and diffusion, indicating high reaction kinetics. Additionally, the relative contributions of capacitance-controlled (k_1) and diffusion-controlled (k_2) behaviour can be quantitatively determined using eqn (2):

$$i(V) = k_1 v + k_2 v^{1/2} \quad (2)$$

As shown in Fig. S14b (SI), the pseudocapacitive contribution to the current increases with the scan rate, rising from 48.02% at 0.4 mV s^{-1} to 67.72% at 1.2 mV s^{-1}, demonstrating the excellent high-rate performance of NHVO-M_x. The prominent surface capacitive contribution is likely due to the low crystallinity structure and larger interlayer spacing, which enhance the utilization of the electrochemically active surface. Moreover, the intercalation of NH_4^+ and doping of metal ions into NHVO-M_x reduces its bandgap, improving interface electron transfer and resulting in remarkable high-rate performance and rapid charge–discharge capabilities.

The performance of Zn^{2+} storage in NHVO-M_x was evaluated using a coin-type half-cell. The galvanostatic charge/discharge (GCD) curves of NHVO-M_x at 0.1 A g^{-1} displayed two sloping plateaus, corresponding to the oxidation and reduction peaks observed in the CV curves (Fig. S15, SI). The specific capacity of the NHVO-M_x cathode increased from 398.1 mAh g^{-1} in the first cycle to 454.4 mAh g^{-1} in the tenth cycle, indicating excellent energy storage capacity. The significant increase in capacity is primarily attributed to the acti-

vation of active materials during the cycling process, along with the gradual infiltration of electrolyte into the interlayers, which enhances the utilization of internal active materials.[37,38] Fig. 4e and Fig. S4 (SI) show the rate performance of the NHVO-M_x, NHVO, and V_2O_5 cathodes. It is evident that NH_4^+ insertion and multi-element doping significantly enhance both the capacity and rate performance of the electrode. At current densities of 0.2, 0.5, 1.0, 2.0, 4.0, 6.0, and 8.0 A g^{-1}, the reversible discharge capacities of the NHVO-M_x were 439.1, 404.8, 371, 327.5, 281.4, 254.5, and 235.7 mAh g^{-1}, respectively. After the rate test, when the current density was returned to 0.2 A g^{-1}, the discharge capacity increased to 464.1 mAh g^{-1}, showing excellent capacity retention. Notably, the synergistic effects of multi-metal doping and NH_4^+ intercalation enhanced the electrochemical kinetics of vanadium oxides, leading to improved and stabilized Zn^{2+} storage and demonstrating superior performance compared to other reported doped vanadium-based cathodes (Fig. 4f).[22,23,29,30,39–45] The Ragone plot showed that the NHVO-M_x delivered stable and superior energy density across a wide range of power densities in aqueous zinc-ion batteries (Fig. S16, SI). For instance, it achieved an energy density of 298.0 Wh kg^{-1} at a power density of 778.1 W kg^{-1}. Cycling stability tests further demonstrated that the NHVO-M_x electrode retained 86.6% of its capacity after 3000 cycles at 8.0 A g^{-1} (Fig. 4g). In contrast, the V_2O_5 electrode underwent rapid degradation during cycling (Fig. S17, SI). This suggested that the large interlayer spacing with NH_4^+ intercalation and low crystallinity structure, produced by low-temperature calcination, alleviated structural stress from zinc ion (de)intercalation, thus maintaining a stable framework. The long-term cycling performance at 0.2, 0.5, and 1 A g^{-1} showed that NHVO-M_x retained 94.4%, 96.0%, and 93.8% of its capacity after 100, 250, and 600 cycles, respectively (Fig. S18, SI). Fig. 4h shows the performance of the NHVO-M_x material assembled in a pouch cell, demonstrating a capacity of 389.4 mAh at 0.2 A g^{-1}. When the current density increases to 0.5 A g^{-1}, the material retains a capacity of 321.6 mAh.

To investigate the electrochemical stability of NHVO-M_x and its zinc storage mechanism during cycling, *ex situ* X-ray diffraction (XRD) was employed to observe the structural evolution of the cathode during charge and discharge. The main structure of NHVO-M_x remained unchanged during cycling, indicating that the primary structure for Zn^{2+} storage was stable. Characteristic peaks shifted to lower 2θ values during discharge and returned to higher 2θ values during charge, indicating reversible insertion and extraction of Zn^{2+} (Fig. 5a). A weak $Zn_3(OH)_2V_2O_7{\cdot}2H_2O$ (ZVO) peak appeared at 0.2 V during dis-

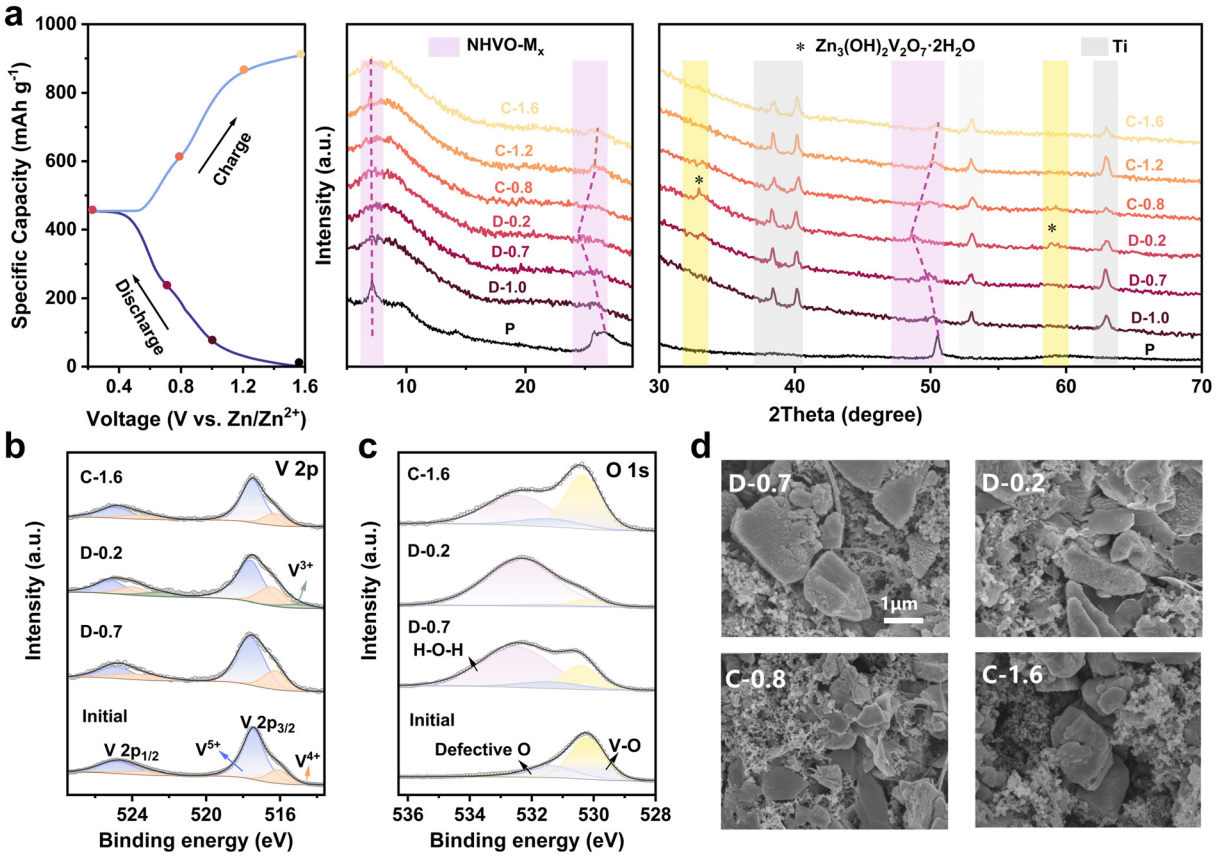

Fig. 5 Energy storage mechanism of NHVO-M_x. (a) *Ex situ* XRD patterns during the charging and discharging processes. (b and c) *Ex situ* XPS spectra of NHVO-M_x: (b) V 2p and (c) O 1s. (d) SEM images of the cathode during the charging and discharging processes.

charge and disappeared at 1.6 V during charge, which may be related to reversible (de-)insertion of protons.[46] Further analysis revealed that single-layer orthorhombic V_2O_5, with low initial capacity, underwent electrochemical activation to transform into $Zn_xV_2O_5{\cdot}nH_2O$, expanding the interlayer spacing from 4.4 Å to 11.8 Å and increasing capacity (Fig. S19 and 20, SI). However, the accumulation of zinc ions between the layers induced significant structural stress, leading to a rapid decline in performance during cycling. In contrast, NHVO-M_x, with NH_4^+ ions, maintained a large interlayer spacing and a stable, open framework structure, resulting in excellent cycling stability.

To explore the electronic structure changes during Zn^{2+} storage, *ex situ* XPS was used to observe the variations in the NHVO-M_x cathode during cycling. The V 2p XPS spectra revealed a two-electron reduction from V^{5+} to V^{3+} during discharge and a reversible oxidation during charge, which contributed to the high energy density of NHVO-M_x (Fig. 5b). Importantly, the intensity of the crystallized water peak in the O 1s spectrum increased in the fully discharged state and decreased in the fully charged state, suggesting that crystallized water enters the interlayer during cycling (Fig. 5c). The interlayer distance of approximately 12.3 Å allowed hydrated zinc ions to diffuse directly between layers, weakening their interaction with the framework and facilitating the reversible insertion and extraction of zinc ions. Thus, NHVO-M_x demonstrated excellent reversible charge–discharge performance. SEM images showed no significant morphological changes during the charge–discharge process, confirming its cycling stability, and EDS provided additional evidence for the uniform insertion of zinc ions during the cycling process (Fig. 5d and Fig. S21, SI).

Environmental and economic assessments

To highlight the significance of the short-process synthesis of high-performance vanadium-based cathodes from vanadium slag leachate, a multi-objective assessment was conducted, including comprehensive environmental, carbon emission, and economic assessments.[47] This study defines the functional unit as the production of 1 kg of doped vanadium oxide electrode material in Sichuan, China. The assessment covers the entire production process, from the raw materials (alkaline leachate of vanadium slag) to the synthesis of cathode active materials (doped vanadium oxide electrode materials) for aqueous zinc batteries. The short-process synthesis method and two traditional production processes were evaluated from environmental and economic perspectives. The two conventional methods are the multi-step precipitation and extraction techniques, followed by hydrothermal synthesis with the addition of dopants (PI and PII, Fig. 6a). In contrast, our streamlined production process involves only targeted impurity removal, vanadium precipitation and low-temperature calcination (PIII, Fig. 6a). The production process is divided into three stages: pretreatment (SI), purification (SII), and product production (SIII). The system boundaries are illustrated in Fig. S22–24 (SI), while the material and energy flows are presented in Fig. S25–27 and Tables S7–9 (SI). A detailed description of the assessment is provided in the Experimental section (SI).

Compared to traditional strategies, the short-process approach results in minimal comprehensive environmental impact (TCEA). PI has the greatest environmental impact, primarily due to the wastewater from multiple precipitation stages. The main pollutants are ranked in the following order of impact:

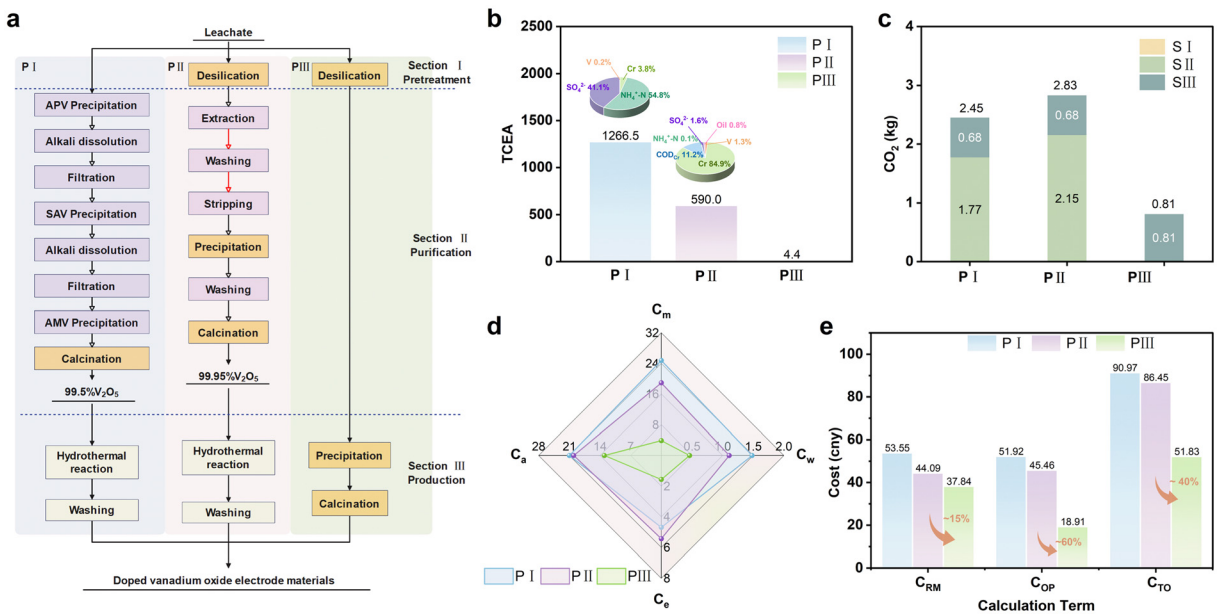

Fig. 6 Multi-objective assessment of the green low-carbon strategy. (a) System boundaries of the low-carbon short process strategy for preparing doped vanadium oxide materials and two traditional strategies. (b) Comprehensive environmental assessment. (c) Carbon emission equivalents at different stages. (d) Cost comparison of different types in the three production processes. (e) Macro-economic cost comparison.

NH_4^+–N > SO_4^{2-} > Cr. For the extraction stage of PII, the environmental impact of the major pollutants follows this order: Cr > COD > SO_4^{2-} > V (Fig. 6b and Tables S10–12, SI). Moreover, a reduction in carbon dioxide equivalent emissions was achieved with the short-process strategy involving doped V_2O_5, mainly due to lower electrical and thermal energy consumption associated with the purification process. As a result, the carbon dioxide equivalent emissions for the entire production process decreased significantly, from 2.45 kg for process PI and 2.83 kg for process PII to 0.81 kg (Fig. 6c). Therefore, the short-process method using leachate is considered a more environmentally friendly and carbon-reducing approach for synthesizing doping-modified vanadium-based cathodes.

Economic evaluation is a crucial aspect of assessing production processes. Cost analysis revealed that the short-process method results in cost reductions in raw material, pretreatment, and purification stages, particularly due to the elimination of complex impurity removal (Fig. S28, SI). Compared to the traditional route, the short-process approach approximately cuts energy costs by 70%, water costs by 60%, materials costs by 80%, and auxiliary costs by 65% (Fig. 6d and Fig. S29, SI). On a macro scale, reducing material losses lowers the need for initial leachate, which leads to an approximately 15% reduction in raw materials costs. Operational costs (materials, energy, and water) are reduced by about 60%, resulting in a reduction of about 40% in total costs compared to traditional methods, reaching only 51.83 CNY per kg (Fig. 6e). In summary, the short-process method utilizing vanadium slag leachate offers a simpler and more efficient synthesis pathway with reduced material and energy inputs. This not only cuts costs but also lowers pollution and carbon emissions, significantly minimizing environmental impact. This strategy aims to provide valuable insights for the development of sustainable next-generation battery materials.

Conclusions

In summary, we developed a low-carbon, short-process method for preparing NH_4^+-intercalated and multi-element-doped vanadium oxides from vanadium slag leachate as high-performance cathodes for AZIBs. By targeting impurity removal, beneficial impurities are used as dopants, while process steps are minimized. Additionally, a low-temperature, oxygen-free calcination reduces carbon emissions and preserves essential NH_4^+ intercalation. This synergy enhances the crystal and electronic structures: NH_4^+ expands the interlayer spacing to facilitate Zn^{2+} ion diffusion, while both NH_4^+ intercalation and multi-element doping narrow the band gap, improving interface charge transfer. As a result, the NHVO-M_x material exhibits excellent zinc storage performance, with a high capacity of 454.4 mAh g^{-1} at 0.1 A g^{-1} and exceptional cycling stability over 3000 cycles at 8 A g^{-1}. A multi-objective assessment shows that this short-process strategy not only delivers superior performance but also minimizes environmental impact, reduces carbon emissions, and lowers costs. Moreover, recycling vanadium from waste promotes sustainable metal resource utilization and advances cleaner, high-performance materials for AZIBs.

Author contributions

L. G., P. N., and H. C. conceptualized the research. L. G. conducted the experiments and wrote the initial manuscript. W. J., G. X., and J. Z. helped design certain experimental methods and offered suggestions on the manuscript. L. G., P. N., and H. C. played key roles in analysing and editing the paper. All authors reviewed the results and contributed to the work.

Conflicts of interest

The authors declare no conflict of interest.

Data availability

The data supporting this article have been included as part of the supplementary information (SI). The supplementary information provides detailed experimental procedures, including the reagents and parameters used. It also contains the data sources and comprehensive characterization data. Supplementary information is available. See DOI: https://doi.org/10.1039/d5eb00146c.

Acknowledgements

This work was supported by the National Key R&D Program of China, Grant No. 2023YFC2908304; and the 14th Five-year Informatization Plan of Chinese Academy of Sciences, Construction of Scientific Data Centre System, Grant No. WX145XQ07-12.

References

1 S. Mallapaty, *Nature*, 2020, **586**, 482–483.
2 S. Chu and A. Majumdar, *Nature*, 2012, **488**, 294–303.
3 D. Larcher and J.-M. Tarascon, *Nat. Chem.*, 2015, **7**, 19–29.
4 S. W. D. Gourley, R. Brown, B. D. Adams and D. Higgins, *Joule*, 2023, **7**, 1415–1436.
5 B. Tang, L. Shan, S. Liang and J. Zhou, *Energy Environ. Sci.*, 2019, **12**, 3288–3304.
6 X. Wang, Z. Zhang, B. Xi, W. Chen, Y. Jia, J. Feng and S. Xiong, *ACS Nano*, 2021, **15**, 9244–9272.
7 L. E. Blanc, D. Kundu and L. F. Nazar, *Joule*, 2020, **4**, 771–799.
8 S. Bi, S. Wang, F. Yue, Z. Tie and Z. Niu, *Nat. Commun.*, 2021, **12**, 6991.
9 M. Yang, Y. Wang, D. Ma, J. Zhu, H. Mi, Z. Zhang, B. Wu, L. Zeng, M. Chen, J. Chen and P. Zhang, *Angew. Chem.*, 2023, **135**, e202304400.

10 Y. Yuan, R. Sharpe, K. He, C. Li, M. T. Saray, T. Liu, W. Yao, M. Cheng, H. Jin, S. Wang, K. Amine, R. Shahbazian-Yassar, M. S. Islam and J. Lu, *Nat. Sustainability*, 2022, **5**, 890–898.
11 X. Ma, X. Cao, M. Yao, L. Shan, X. Shi, G. Fang, A. Pan, B. Lu, J. Zhou and S. Liang, *Adv. Mater.*, 2022, **34**, 2105452.
12 D. Kundu, B. D. Adams, V. Duffort, S. H. Vajargah and L. F. Nazar, *Nat. Energy*, 2016, **1**, 1–8.
13 Z. Song, L. Miao, L. Ruhlmann, Y. Lv, L. Li, L. Gan and M. Liu, *Angew. Chem., Int. Ed.*, 2023, **62**, e202219136.
14 D. Qin, J. Ding, C. Liang, Q. Liu, L. Feng, Y. Luo, G. Hu, J. Luo and X. Liu, *Acta Phys.-Chim. Sin.*, 2024, **40**, 2310034.
15 M. Liu, B. Su, Y. Tang, X. Jiang and A. Yu, *Adv. Energy Mater.*, 2017, **7**, 1700885.
16 X. Zeng, Z. Gong, C. Wang, P. J. Cullen and Z. Pei, *Adv. Energy Mater.*, 2024, **14**, 2401704.
17 Y. Liu, Y. Jiang, Z. Hu, J. Peng, W. Lai, D. Wu, S. Zuo, J. Zhang, B. Chen, Z. Dai, Y. Yang, Y. Huang, W. Zhang, W. Zhao, W. Zhang, L. Wang and S. Chou, *Adv. Funct. Mater.*, 2021, **31**, 2008033.
18 H. Tang, Z. Peng, L. Wu, F. Xiong, C. Pei, Q. An and L. Mai, *Electrochem. Energy Rev.*, 2018, **1**, 169–199.
19 P. Ruan, S. Liang, B. Lu, H. J. Fan and J. Zhou, *Angew. Chem., Int. Ed.*, 2022, **61**, e202200598.
20 L. Wang, J. Yan, Y. Hong, Z. Yu, J. Chen and J. Zheng, *Sci. Adv.*, 2023, **9**, eadf4589.
21 Y. Yang, Y. Tang, G. Fang, L. Shan, J. Guo, W. Zhang, C. Wang, L. Wang, J. Zhou and S. Liang, *Energy Environ. Sci.*, 2018, **11**, 3157–3162.
22 P. He, G. Zhang, X. Liao, M. Yan, X. Xu, Q. An, J. Liu and L. Mai, *Adv. Energy Mater.*, 2018, **8**, 1702463.
23 F. Ming, H. Liang, Y. Lei, S. Kandambeth, M. Eddaoudi and H. N. Alshareef, *ACS Energy Lett.*, 2018, **3**, 2602–2609.
24 C. Xia, J. Guo, P. Li, X. Zhang and H. N. Alshareef, *Angew. Chem., Int. Ed.*, 2018, **57**, 3943–3948.
25 J. Zheng, C. Liu, M. Tian, X. Jia, E. P. Jahrman, G. T. Seidler, S. Zhang, Y. Liu, Y. Zhang, C. Meng and G. Cao, *Nano Energy*, 2020, **70**, 104519.
26 J. Guo, B. He, W. Gong, S. Xu, P. Xue, C. Li, Y. Sun, C. Wang, L. Wei, Q. Zhang and Q. Li, *Adv. Mater.*, 2024, **36**, 2303906.
27 C. Liu, Z. Neale, J. Zheng, X. Jia, J. Huang, M. Yan, M. Tian, M. Wang, J. Yang and G. Cao, *Energy Environ. Sci.*, 2019, **12**, 2273–2285.
28 T. Lv, G. Zhu, S. Dong, Q. Kong, Y. Peng, S. Jiang, G. Zhang, Z. Yang, S. Yang, X. Dong, H. Pang and Y. Zhang, *Angew. Chem., Int. Ed.*, 2023, **62**, e202216089.
29 M. Du, C. Liu, F. Zhang, W. Dong, X. Zhang, Y. Sang, J.-J. Wang, Y.-G. Guo, H. Liu and S. Wang, *Adv. Sci.*, 2020, **7**, 2000083.
30 C. Zhang, Y. Huang, X. Xu, Z. Chen, G. Xiao, Y. Zhong, X. Wang, C. Gu and J. Tu, *Energy Environ. Sci.*, 2024, **17**, 4090–4103.
31 S. Li, X. Xu, K. Wang, W. Chen, X. Lu, Z. Song, J.-Y. Hwang, J. Kim, Y. Bai, Y. Liu and S. Xiong, *ACS Energy Lett.*, 2022, **7**, 3770–3779.
32 Y.-H. Wang, Y.-F. Wang, Y.-T. Li, C. Wu, X.-L. Han, N.-N. Zhao, Z.-K. Zhang, L. Dai, L. Wang and Z.-X. He, *Rare Met.*, 2024, **43**, 4115–4131.
33 P. Hu, Y. Zhang, H. Liu, T. Liu, S. Li, R. Zhang and Z. Guo, *Sep. Purif. Technol.*, 2023, **304**, 122319.
34 S. Liu, L. Wang, J. Chen, L. Ye and J. Du, *Sep. Purif. Technol.*, 2024, **342**, 127035.
35 Y. Wang, S. Wei, Z.-H. Qi, S. Chen, K. Zhu, H. Ding, Y. Cao, Q. Zhou, C. Wang, P. Zhang, X. Guo, X. Yang, X. Wu and L. Song, *Proc. Natl. Acad. Sci. U. S. A.*, 2023, **120**, e2217208120.
36 S. Deng, Z. Yuan, Z. Tie, C. Wang, L. Song and Z. Niu, *Angew. Chem., Int. Ed.*, 2020, **59**, 22002–22006.
37 X. Liang, L. Yan, W. Li, Y. Bai, C. Zhu, Y. Qiang, B. Xiong, B. Xiang and X. Zou, *Nano Energy*, 2021, **87**, 106164.
38 J. He, X. Liu, H. Zhang, Z. Yang, X. Shi, Q. Liu and X. Lu, *ChemSusChem*, 2020, **13**, 1568–1574.
39 H. Geng, M. Cheng, B. Wang, Y. Yang, Y. Zhang and C. C. Li, *Adv. Funct. Mater.*, 2020, **30**, 1907684.
40 F. Wu, Y. Wang, P. Ruan, X. Niu, D. Zheng, X. Xu, X. Gao, Y. Cai, W. Liu, W. Shi and X. Cao, *Mater. Today Energy*, 2021, **21**, 100842.
41 H. Yang, P. Ning, Z. Zhu, L. Yuan, W. Jia, J. Wen, G. Xu, Y. Li and H. Cao, *Chem. Eng. J.*, 2022, **438**, 135495.
42 P. Luo, Z. Huang, G. Liu, C. Liu, P. Zhang, Y. Xiao, W. Tang, W. Zhang, H. Tang and S. Dong, *J. Alloys Compd.*, 2022, **919**, 165804.
43 Z.-H. Su, R.-H. Wang, J.-H. Huang, R. Sun, Z.-X. Qin, Y.-F. Zhang and H.-S. Fan, *Rare Met.*, 2022, **41**, 2844–2852.
44 J. Cao, D. Zhang, Y. Yue, X. Wang, T. Pakornchote, T. Bovornratanaraks, X. Zhang, Z.-S. Wu and J. Qin, *Nano Energy*, 2021, **84**, 105876.
45 T. Zhou, X. Du and G. Gao, *J. Energy Chem.*, 2024, **95**, 9–19.
46 L. Wang, K.-W. Huang, J. Chen and J. Zheng, *Sci. Adv.*, 2019, **5**, eaax4279.
47 G. Zhang, Y. Wang, X. Meng, D. Zhang, N. Ding, Z. Ren, W. Gao and Z. Sun, *Resour., Conserv. Recycl.*, 2023, **192**, 106926.